Identification of the Protonated Oxygenic Ligands of Ribonucleotide Reductase Intermediate X by Q-Band ^{1,2}H CW and Pulsed ENDOR

Jean-Paul Willems,[†] Hong-In Lee,[†] Doug Burdi,[‡] Peter E. Doan,[†] JoAnne Stubbe,*[,‡] and Brian M. Hoffman*[,†]

Contribution from the Departments of Chemistry, Northwestern University, Evanston, Illinois 60208-3113, and MIT, Cambridge, Massachusetts 02139-4307

Received March 28, 1997. Revised Manuscript Received June 27, 1997[⊗]

Abstract: We report CW and pulsed Q-band ^{1,2}H ENDOR measurements of intermediate **X** formed during the assembly of the diferric tyrosyl radical cofactor of the R2 subunit in ribonucleotide reductase. These studies, performed with H_2O and D_2O buffers, were designed to determine whether the exchangeable proton signals are associated with an hydroxo bridge, a terminal water, or both. In doing so, we identify the types of protonated oxygen (OH_x) species coordinated to the iron ions of **X** and their disposition relative to the ferric and ferryl iron ions. The exchangeable proton signals displayed by intermediate **X** belong to two protons associated with a terminal water bound to Fe^{III} and not to an hydroxo bridge; within the precision of the modeling, this picture of a terminal water is indistinguishable from that of a 2-fold disordered terminal hydroxyl. The fact that **X** displays strong spin-coupling between iron ions requires that there be one or more oxo/hydroxo bridges. These findings then establish that **X** contains the $[(H_xO)Fe^{III}OFe^{IV}]$ fragment.

Introduction

The non-heme diiron enzymes have attracted keen interest by their diverse chemical reactivity toward dioxygen.[1,2] Reversible oxygen-binding of the diferrous form of hemerythrin (Hr)[3] may be contrasted with oxygen activation by the diferrous forms of methane monooxygenase (MMO) and of the R2 subunit of *Escherichia coli* ribonucleotide reductase (RNR). Reductive O_2 activation in MMO generates a species that is capable of oxidizing methane to methanol, while in R2 one is formed that oxidizes an adjacent tyrosine to a tyrosyl radical. Despite the availability of X-ray crystallographic analyses, which show that the diiron centers of MMO[4] and R2[5] have oxygen-rich primary coordination spheres, in contrast to the nitrogen-rich coordination in Hr,[6] the basis for the differences in reactivity toward O_2 remains unknown, and its discovery is the focus of many laboratories.

The intermediates along the pathways leading to oxygen activation in both MMO and R2 have been the subject of recent physical−biochemical investigations employing time-resolved experiments. Among the earliest species detected in the reaction of diferrous MMO with dioxygen is a putative symmetrical diferric peroxide, designated **P**,[7,8] whose proposed structure is based on its symmetrical Mössbauer spectrum ($\delta = 0.66$ mm s^{-1})[9] and an $^{16}O-^{18}O$-sensitive stretch in its resonance Raman spectrum.[10] Intermediate **P** is converted to a second intermediate, **Q**, that is catalytically competent to oxidize methane into methanol. The isomer shift(s) observed in the Mössbauer spectra of **Q** from the MMO in *Methylosinus trichosporium* ($\delta = 0.17$ mm s^{-1})[11] and *Methyloccus capsulatus* (Bath) ($\delta_1 = 0.21$ mm s^{-1}, $\delta_2 = 0.14$ mm s^{-1})[10] have been interpreted to support the presence of a diiron(IV) cluster. The recent determination by EXAFS spectroscopy[12] that **Q** has a short (2.5 Å) iron−iron separation has prompted its description as a "diamond core" di-μ-oxo-bridged diiron(IV) complex.

The diiron center in the R2 subunit plays no role in the nucleotide reduction process catalyzed by RNR but is required to generate the diferric cluster/tyrosyl radical (·Y122) cofactor[13,14] that is essential to the catalytic mechanism of nucleotide reduction. The time course of the reaction of apo-R2 with Fe^{II}, O_2, and reductant, and that of diferrous R2 with O_2, have been studied using stopped-flow UV−vis spectroscopy in conjunction with rapid freeze−quench (RFQ) EPR and Mössbauer spectroscopies.[15] In the former case, a paramagnetic diiron intermediate (**X**) has been observed that is one-electron-oxidized above the diferric resting state and is catalytically competent to oxidize tyrosine to tyrosyl radical.[16] The use of a site-directed

[†] Northwestern University.
[‡] MIT.
[⊗] Abstract published in *Advance ACS Abstracts,* September 15, 1997.

(1) Feig, A. L.; Lippard, S. J. *Chem. Rev.* **1994**, *94*, 759−805.
(2) Wallar, B. J.; Lipscomb, J. D. *Chem. Rev.* **1996**, *96*, 2625−2657.
(3) Shiemke, A. K.; Sanders-Loehr, T. M.; Sanders-Loehr, J. *J. Am. Chem. Soc.* **1986**, *108*, 2437−2443.
(4) Rosenzweig, A. C.; Nordlund, P.; Takahara, P. M.; Frederick, C. A.; Lippard, S. J. *Chem. Biol.* **1995**, *2*, 409−418.
(5) Logan, D. T.; Su, X.-D.; Åberg, A.; Regnström, K.; Hajdu, J.; Eklund, H.; Nordlund, P. *Structure* **1996**, *4*, 1053−1064.
(6) Holmes, M. A.; LeTrong, I.; Turley, S.; Sieker, L. C.; Stenkamp, K. E. *J. Mol. Biol.* **1991**, *218*, 583−593.
(7) Kiu, K. E.; Valentine, A. M.; Wang, D.; Huynh, B. H.; Edmondson, D. E.; Salifoglou, A.; Lippard, S. J. *J. Am. Chem. Soc.* **1995**, *117*, 10174−10185.
(8) Lee, S.-K.; Nesheim, J. C.; Lipscomb, J. D. *J. Biol. Chem.* **1993**, *268*, 21569−21577.
(9) Liu, K. E.; Wang, D.; Huynh, B. H.; Edmondson, D. E.; Salifoglou, A.; Lippard, S. J. *J. Am. Chem. Soc.* **1994**, *116*, 7465−7466.
(10) Liu, K. E.; Valentine, A. M.; Qiu, D.; Edmondson, D. E.; Appelman, E. H.; Spiro, T. G.; Lippard, S. J. *J. Am. Chem. Soc.* **1995**, *117*, 4997−4998.
(11) Lee, S.-K.; Fox, B. G.; Froland, W. A.; Lipscomb, J. D.; Münck, E. *J. Am. Chem. Soc.* **1993**, *115*, 6450−6451.
(12) Shu, L.; Nesheim, J. C.; Kauffmann, K.; Münck, E.; Lipscomb, J. D.; Que, L., Jr. *Science* **1997**, *275*, 515−518.
(13) Atkin, C. L.; Thelander, L.; Reichard, P.; Lang, G. *J. Biol. Chem.* **1973**, *248*, 7464−7472.
(14) Larsson, Å.; Sjöberg, B.-M. *EMBO J.* **1986**, *5*, 2037−2040.
(15) Bollinger, J. M., Jr.; Edmondson, D. E.; Huynh, B. H.; Filley, J.; Norton, J. R.; Stubbe, J. *Science* **1991**, *253*, 292−298.
(16) Bollinger, J. M., Jr.; Tong, W. H.; Ravi, N.; Huynh, B. H.; Edmondson, D. E.; Stubbe, J. *J. Am. Chem. Soc.* **1994**, *116*, 8015−8023.

S0002-7863(97)00994-3 CCC: $14.00

mutant, Y122F, has shown that **X** can be generated in stoichiometric amounts[15,17] in the absence of a tyrosyl radical, facilitating its characterization. Recent Mössbauer[17] and stopped-flow[18] studies of the wild-type protein have observed an intermediate prior to **X** whose properties resemble those of the diferric peroxide **P** seen in MMO. The chemical basis for the conversion of **P** into **Q** in MMO, in contrast to the conversion of a similar species into **X** in R2, remains to be elucidated. Our recent EXAFS findings,[18] that **X** contains an Fe−Fe distance of 2.5 Å in both mutant and wild-type proteins, raise the question of whether **X** contains a diamond core motif similar to that proposed for **Q**.

The paramagnetism of **X**, in contrast to the diamagnetism of both **P** and **Q**, means that the study of **X** by EPR and ENDOR[19] methods affords an unmatched opportunity to determine the fate of O_2 during the formation of an intermediate in the reductive activation of dioxygen with a non-heme diiron center. In order to define the composition and structure of **X**, we have extended the RFQ technique to Q-band ENDOR spectroscopy. An ^{57}Fe ENDOR study[20a] clarified the electronic properties of the diiron center of **X** and offered a revised spin-coupling paradigm which describes **X** as having an $S = {}^1/_2$ diiron center with antiferromagnetic coupling between Fe^{III} ($S = {}^5/_2$) and Fe^{IV} ($S = 2$) ions. The observed antiferromagnetic exchange-coupling between iron ions requires the presence of one or more oxy and/or hydroxo bridges. A preliminary Q-band CW ENDOR study of **X** by Burdi et al.[20b] using $^{17}O_2$ and $H_2{}^{17}O$ corroborated the earlier observation of ^{17}O coupling by X-band EPR[21] and demonstrated the presence of one oxygen ligand derived from solvent and at least one from dioxygen. The same report also presented a limited 2-D set of orientation-selective CW Q-band ^{1}H ENDOR spectra taken at several fields across the EPR envelope of samples of **X** prepared in both H_2O and D_2O buffer. At fields near g_1, a signal was observed from an exchangeable proton or protons having a coupling constant of $A_H = 21$ MHz. The hyperfine tensor was highly anisotropic, with the breadth of the pattern decreasing at lower g values (higher fields). At fields near g_3, the spectra revealed intensity from (an) exchangeable proton(s) having a coupling of $A \approx 9$ MHz. The possible relationship between these two sets of signals was unclear; at intermediate g values, they overlapped with intensity from nonexchangeable protons, and this made H_2O/D_2O subtractions[22] unreliable. Comparison of the orientation-selective proton ENDOR results with those from the mixed-valence state of MMOH and Hr[23] showed a similarity that suggested that the signal of the more strongly coupled proton from **X** might arise from a hydroxo bridge, and the other signal from the proton(s) of a terminally bound aqua species. A subsequent CW X-band study[24] concluded that the exchangeable protons were associated with a hydroxo bridge. However, further analysis by us has disclosed that the two types of signals probably arise from a single type of hydrogenic species, and that not even the superior

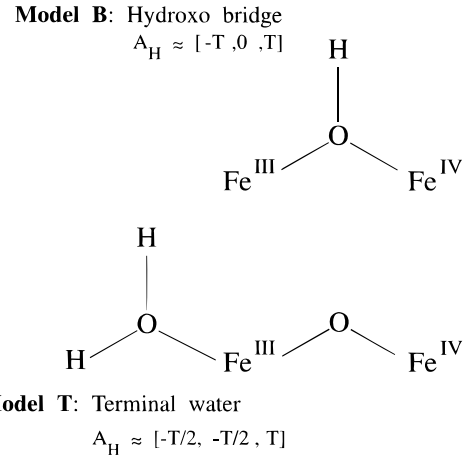

Figure 1. Alternate, partial models for exogenous ligands to intermediate **X**. Top, hydroxo bridge (**B** model); bottom, oxo bridge plus terminal water (**T** model). Approximate characteristics of the cluster dipolar hyperfine tensors are indicated (eqs A1−A3).

orientation selection of the published CW data collected at Q band allows a distinction between the two models sketched in Figure 1. In one model, which we denote **B**, all exchangeable proton/deuteron signals with substantial couplings are assigned to a hydroxo bridge; in the other, denoted **T**, these signals are assigned to the two protons of a water molecule bound to Fe^{III}. The number and nature of OH_x ligand(s) to the diiron center of **X** thus remained undetermined.

We now report CW and pulsed Q-band ^{1,2}H ENDOR measurements of intermediate **X** in the cofactor assembly of the R2 subunit of ribonucleotide reductase, in H_2O and D_2O buffers. These were designed to determine whether the exchangeable proton signals are associated with a hydroxo bridge, a terminal water, or both. In doing so, we identify the types of protonated oxygen (OH_x) species coordinated to the iron ions of **X** and their disposition relative to the ferric and ferryl iron ions. This information is an important component in the eventual determination of the fate of the atoms of dioxygen and of the structure of **X**. Given the widespread ability of nonheme diiron centers to bind dioxygen *and* to activate it for reaction,[1,2] the unique opportunity provided by **X** to examine an intermediate in the reaction of dioxygen with a non-heme diiron center is important for our understanding of all such centers, not only for deducing the mechanism of activation of this enzyme.

Materials and Methods

Preparation of Apo Y122F. R2-Y122F was isolated from the overproducing *E. coli* strain BL21 (DE3)/pTB2 (Y122F) and purified as described previously.[16] Apo-R2-Y122F was prepared from its diferric precursor using a modification[25] of the chelation procedure of Atkin et al.[13] The concentration of apo-R2 was determined by A_{280} (e = 120 mM^{-1} cm^{-1}).[26]

Preparation of RFQ Q-Band ENDOR Samples. RFQ ENDOR samples were prepared as previously described.[27] A quench time of 610 ms was selected. Buffered solutions in H_2O were prepared by the addition of HEPES (23.8 g, 100 mmol) to H_2O (1 L) and adjusting the pH to a meter reading of 7.7 using 5 M NaOH. Buffered solutions in ^2H_2O were prepared by the addition of HEPES (1.19 g, 5 mmol) to ^2H_2O (50 mL) and adjusting the pH to a meter reading of 7.3 using 10 M NaO^2H in ^2H_2O according to the technique of Glasoe and Long.[28] ^2H_2O (99.8%) was purchased from Cambridge Isotope Labs.

(17) Tong, W. H. Ph.D. Thesis, Massachusetts Institute of Technology, 1996.
(18) Riggs-Gelasco, P.; Shu, L.; Chen, S.; Burdi, D.; Huynh, B. H.; Que, L. J.; Stubbe, J. *J. Am. Chem. Soc.*, submitted.
(19) Abragam, A.; Bleaney, B. *Electron Paramagnetic Resonance of Transition Ions*, 2nd ed.; Clarendon Press: Oxford, 1970.
(20) (a) Sturgeon, B. E.; Burdi, D.; Chen, S.; Huynh, B.-H.; Edmondson, D. E.; Stubb, J.; Hoffman, B. M. *J. Am. Chem. Soc.* **1996**, *118*, 7551−7557. (b) Burdi, D.; Sturgeon, B. E.; Tong, W. H.; Stubbe, J.; Hoffman, B. M. *J. Am. Chem. Soc.* **1996**, *118*, 281−282.
(21) Ravi, N.; Bollinger, J. M., Jr.; Huynh, B. H.; Edmondson, D. E.; Stubbe, J. *J. Am. Chem. Soc.* **1994**, *116*, 8007−8014.
(22) Doan, P. E.; Fan, C.; Hoffman, B. M. *J. Am. Chem. Soc.* **1994**, *116*, 1033−1041.
(23) DeRose, V. J.; Liu, K. E.; Lippard, S. J.; Hoffman, B. M. *J. Am. Chem. Soc.* **1996**, *118*, 121−134.
(24) Veselov, A.; Scholes, C. P. *Inorg. Chem.* **1996**, *35*, 3702−3705.
(25) Salowe, S. P. Ph.D. Thesis, University of Wisconsin, 1987.
(26) Thelander, L. *J. Biol. Chem.* **1973**, *248*, 4591−4601.
(27) Sturgeon, B. E.; Burdi, D.; Chen, S.; Huynh, B.-H.; Edmondson, D. E.; Stubbe, J.; Hoffman, B. M. *J. Am. Chem. Soc.* **1996**, *118*, 7551−7557.
(28) Glasoe, P. K.; Long, F. A. *J. Phys. Chem.* **1960**, *64*, 188−190.

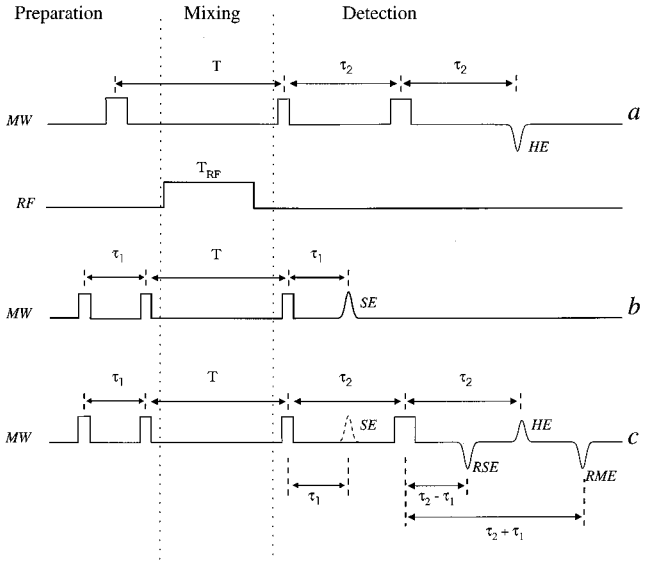

Figure 2. Pulsed ENDOR microwave sequences used in this study: (a) Davies, (b) Mims, and (c) ReMims. The rf sequence is common to all.

ENDOR Spectroscopy. The CW ENDOR spectrometer and procedures employed in this study have been briefly described.[29] A description of the 35 GHz pulse ENDOR spectrometer employed in this study has been published recently.[30] The proton CW ENDOR spectra reported have been recorded using "Packet-Shifting" ENDOR.[31] Although this type of ENDOR has many advantages when studying metalloproteins, including excellent signal/noise ratios, at low sample temperature, where relaxation rates are slow, it also can manifest distortions in peak shapes and intensities. In particular, signals with small hyperfine coupling may not be well-resolved, and those with larger couplings that are resolved exhibit line shapes and intensities that depend on the spectrometer settings, such as microwave power, field modulation amplitude, rf power, and rf scan rate and direction. The CW ^{1}H ENDOR spectra presented in this paper have been taken under conditions, given in the appropriate figure legends, where the shapes match those obtained using the Davies pulsed ENDOR protocol,[32,33] which does give reliable shapes; we note that this was not the case in the original report.[20] The Davies (Figure 2a) ENDOR pulse sequence[32,33] is hyperfine-selective because the ENDOR response, R, is jointly dependent on the hyperfine coupling, A, and the length of the microwave pulse, t_p, in the preparation phase, through the selectivity factor, $\eta = At_p$:

$$R = R_0\left(\frac{1.4\eta}{0.7^2 + \eta^2}\right)$$

where R_0 is the maximum ENDOR response.[34] The equation shows that an optimal ENDOR response is obtained if $\eta = At_p = 0.7$; when $\eta < 0.7$, the response is suppressed. For a given sample, the value of t_p cannot be lengthened beyond some *intrinsic* maximum, t_p^{max}, because dephasing during the pulse diminishes or abolishes the spin-echo observed in the detection phase of the experiment. As a result, the smallest hyperfine coupling, A^{min}, that can be observed with sufficient signal/noise ratios using a Davies ENDOR sequence is roughly $A^{min} \approx 1/t_p^{max}$.

Deuterium ENDOR spectra were collected using the Mims stimulated-echo ENDOR pulse sequence[32,35] (Figure 2b). This protocol also is hyperfine-selective because its ENDOR response R depends jointly on the nuclear hyperfine coupling A and the interval τ according to

$$R \propto [1 - \cos(2\pi A\tau)] \quad (1)$$

This equation shows that the ENDOR response will fall to zero for $A\tau = n = 1, 2, ...$ and will reach a maximum for $n = 0.5, 1.5, ...$ Such "hyperfine selectivity" normally is considered as one of the key benefits of pulsed ENDOR techniques. However, orientation-selective ENDOR analysis of frozen solutions relies on accurate line shapes and intensities. Our experience with Mims ENDOR of powder or frozen solution samples shows that one obtains ENDOR pattern essentially undistorted by the blind spots only for couplings in the range $A < 1/(2\tau)$.[22] Thus, *in practice*, in the study of frozen solutions, the maximum hyperfine value, A^{max}, that should be studied using a Mims ENDOR sequence is restricted by the minimum usable value of τ, denoted as the deadtime, t_d, with the result that $A^{max} \approx 1/(2t_d)$. The deadtime is defined as the minimum time after the last pulse that the ENDOR effect can be detected against the resonator ringdown, and it depends not only on the spectrometer performance but also on the strength of the ENDOR signal. If the effective spectrometer deadtime is long, thereby reducing A^{max} in a Mims sequence, or if the sample phase memory is short, thereby increasing A^{min} in a Davies sequence, it is not possible to obtain undistorted spectra for hyperfine couplings that fall in a "gap" defined by $1/(2t_d) < A < 1/t_p^{max}$.

In the case of intermediate **X**, the maximum useful value of t_p typically was of the order of 0.2 μs, which means that an optimized Davies ENDOR response could be achieved for nuclei having hyperfine coupling constants larger than ~3.5 MHz (as will be seen below because of other considerations, the minimum ^{1}H hyperfine coupling that can be well-studied for exchangeable protons is closer to 8 MHz). The effective deadtime of the spectrometer, as configured, was approximately 0.5 μs for the available samples of intermediate **X**. Hence, the maximum hyperfine value accessible using a Mims pulse sequence is roughly 2 MHz. Consequently, for this sample, there, in fact, is a gap, such that signals with hyperfine couplings $2 \lesssim A \lesssim 3.5$ MHz cannot be well-studied by the conventional pulsed ENDOR protocols, and this is crucial for the ^{2}H ENDOR measurements. To fill this gap, we used the recently described Refocused Mims (ReMims) pulse sequence (see Figure 2c).[36] This is a four-pulse stimulated-echo ENDOR variation of the original Mims ENDOR sequence that eliminates the linkage between hyperfine coupling and spectrometer deadtime by permitting experiments where τ is less than the deadtime of the detection system: the hyperfine selectivity is governed by τ according to eq 1, but the deadtime only must be shorter than $\tau_2 + \tau_1$ (see Figure 2c), which can be set to an arbitrary value. The ReMims sequence, therefore, increases the A^{max} of a Mims ENDOR so as to recover the hyperfine values poorly interrogated by both the Davies and Mims ENDOR sequences.

A proton ENDOR signal for a single molecular orientation consists of a doublet centered at the Larmor frequency, ν_H, and split by the hyperfine coupling A_H; spectra in this paper are plotted as $\Delta\nu = \nu - \nu_H$. A deuterium signal consists of a doublet centered at ν_D and split by A_D, with an additional splitting caused by the nuclear quadrupole interaction. The Larmor frequency and hyperfine constants of protons and deuterons are related by the equation $\nu_H/\nu_D = A_H/A_D = g_H/g_D = 6.5$. As discussed in detail,[31,37,38] for a frozen solution sample, the determination of the full hyperfine tensor (and quadrupole tensor) of an interacting nucleus is achieved by obtaining a 2-D set of orientation-selective ENDOR spectra collected at multiple fields across the EPR envelope and comparing this set with simulated 2-D patterns. Although **X** gives an essentially isotropic EPR spectrum at X band, and hence no orientation selection, EPR spectra at Q band show that the **g** tensor is rhombic, with $\mathbf{g} = [g_1, g_2, g_3] \approx [2.0081(5), 1.9977(5), 1.9926(5)]$,[20] which is adequate to allow such an analysis at Q band. The ENDOR simulations were performed on a PC using the program Gensim, a

(29) Werst, M. M.; Davoust, C. E.; Hoffman, B. M. *J. Am. Chem. Soc.* **1991**, *113*, 1533−1538.
(30) Davoust, C. E.; Doan, P. E.; Hoffman, B. M. *J. Magn. Reson., A* **1996**, *119*, 38−44.
(31) DeRose, V. J.; Hoffman, B. M. *Methods Enzymol.* **1995**, *246*, 554−589.
(32) Gemperle, C.; Schweiger, A. *Chem. Rev.* **1991**, *91*, 1481−1505.
(33) Davies, E. R. *Phys. Lett.* **1974**, *47A*, 1−2.
(34) Fan, C.; Doan, P. E.; Davoust, C. E.; Hoffman, B. M. *J. Magn. Reson.* **1992**, *98*, 62−72.
(35) Mims, W. B. *Proc. R. Soc. London* **1965**, *283*, 452−457.
(36) Doan, P. E.; Hoffman, B. M. *Chem. Phys. Lett.* **1997**, *269*, 208−214.
(37) Hoffman, B. M. *Acc. Chem. Res.* **1991**, *24*, 164−170.
(38) Hoffman, B. M.; DeRose, V. J.; Doan, P. E.; Gurbiel, R. J.; Houseman, A. L. P.; Telser, J. In *EMR of Paramagnetic Molecules*; Berliner, L. J., Reuben, J., Eds.; Biological Magnetic Resonance 13; Plenum Press: New York, 1993; pp 151−218.

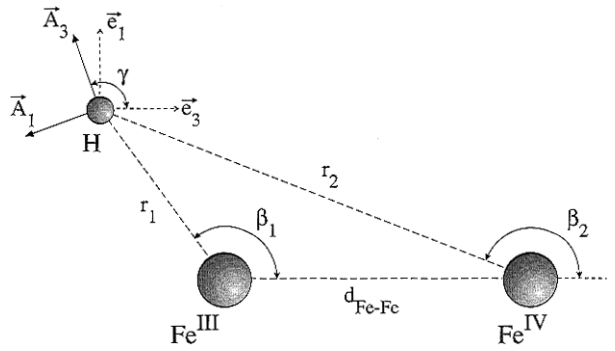

Figure 3. Definition of metrical parameters used in calculation of cluster hyperfine tensor **A (**eqs A1−A3).

modified version of the simulation program GENDOR,[38] which speeds calculations when orientation selectivity is poor, as in the case of intermediate **X**.

Results

Alternative Models for the Protonated Oxygenic Species of Intermediate X. The preliminary ^{1}H and ^{17}O ENDOR measurements of Burdi et al.[20b] clearly demonstrated the presence of signals from exchangeable proton or protons associated with a hydroxo bridge (Figure 1, top), a terminal water (Figure 1, bottom), or both. This section presents ^{1,2}H ENDOR spectra calculated for the two different models using parameters for each that are chosen to optimize the agreement with experiments presented below. The similarities and differences between the two sets of calculations are carefully noted in preparation for comparison with the experiments.

Our prior work[23,39,40] shows that the protons of a bridge and of a terminal water both exhibit dipolar interactions with an interacting Fe ion. The Appendix gives equations for the observed cluster hyperfine tensor of a proton that is dipole-coupled to the $S = {}^1/_2$ ground state of a spin-coupled [Fe($S = {}^5/_2$)−Fe($S = 2$)] diiron center. The equations apply to a nucleus that occupies an arbitrary position relative to the two Fe ions and are functions of the cluster's metrical parameters as defined in Figure 3; a limiting form of this treatment, appropriate only for a bridge, was given in a discussion of the (Fe^{III}−Fe^{II}) clusters of "mixed-valence" MMOH.[23] Figure 4 presents the values of the principal components of the hyperfine tensor that are the largest (A_3) and smallest in *magnitude* (A_2), given in a representative contour plot as a function of r_1 and β_1 for a fixed Fe^{III}−Fe^{IV} separation, as defined in Figure 3. For a terminal water (or hydroxide), where the proton is positioned either so that $\beta_1 > 90°$ or $\beta_2 < 90°$ (Figure 3), then the dipole interaction with the liganding iron dominates the ^{1,2}H hyperfine tensor, which is approximately axial: $\mathbf{A} \approx [-{}^1/_2T, -{}^1/_2T, T]$. The A_3 axis lies close to the Fe−H vector, and $T \approx (7/3)g\beta g_n\beta_n/r_1^3$ when the ligand is bound to the ferric ion and $\beta_1 > 90°$, but $T \approx (-{}^4/_3)g\beta g_n\beta_n/r_2^3$ when it is bound to the ferryl ion and $\beta_2 < 90°$ (See Appendix). In contrast, a proton of a bridging hydroxide interacts strongly with both Fe ions, and it is characterized by a nearly rhombic hyperfine tensor, $\mathbf{A} \approx [-T, 0, T]$, where A_2 lies normal to the Fe(H)Fe plane and **A** is rotated about the A_2 direction by the angle γ relative to the cluster axes (eq A3).

Figure 5a presents an optimized 2-D set of ^{1,2}H ENDOR spectra calculated for a proton hyperfine tensor obtained from eq A3 by assuming the presence of a bridging hydroxyl (**B** model) with a dipolar hyperfine interaction to the two iron ions, eq A1. In these calculations, an idealized geometry is assumed in which the O atom is the apex of an isosceles triangle with the two Fe ions and with H in the plane of the other atoms and forming an Fe−H−Fe isosceles triangle. The Fe−Fe separation was chosen to be 2.5 Å. One obtains a hyperfine tensor whose maximum principal component matches the maximum coupling observed experimentally (see below) by selecting an Fe−H distance of ∼2.57 Å and an angle β_1 of ∼70°; this is represented as B in Figure 4. The precise metrical parameters and the hyperfine tensor components are listed in Table 1. Note, however, that the required metrical parameters for the symmetrical bridge include an iron−oxygen distance that is rather short for a bridging hydroxide, ∼1.7 Å. The optimization included the isotropic contribution to the hyperfine tensor as a parameter. As noted in Table 1, the optimized tensor for the **B** model includes a small isotropic component, $A_{iso}(^1H) = 2$ MHz, while those for the **T** model are purely dipolar, $A_{iso} = 0$.

We were prompted by our recent EXAFS data[18] to consider as well a bridge with an unsymmetrically placed hydroxyl, where the Fe^{IV}−O distance is 1.8 Å and Fe^{III}−O is 2.0 Å. However, this model, represented as the (●) point in Figure 4, leads to a longer Fe^{III}−H distance; as a result, its maximum hyperfine component is substantially too small to reproduce the maximum breadth of the proton pattern, near g_1, and its smallest component is far too small to reproduce the smallest breadth of the pattern, near g_3. The largest and smallest widths of the ENDOR pattern can be reproduced by adding a large, negative isotropic term ($A_{iso} = -8$ MHz), which might arise because of spin delocalization onto the bridge, as suggested by the ^{57}Fe ENDOR study of **X**,[27] despite findings that there is no such component for a proton on oxygen bound to a ferric ion or the bridge of an Fe^{III}−Fe^{II} mixed-valence cluster.[23,39,40] However, with the addition of this term, the predictions of the two versions of the **B** model are essentially indistinguishable. Hence, the 2-D set of ^{1,2}H ENDOR spectra displayed in Figure 5a can be regarded as being representative of both the symmetrical and unsymmetrical bridges.

To complete the determination of **A** requires the specification of the Euler angles relating the **A** and **g** tensors. Optimal agreement with experiment (see below) is achieved if A_2 lies along g_3, with g_1 lying roughly between A_1 and A_3; the Euler angles and linewidths used in the calculations of Figure 5 also are given in Table 1. For comparison with the experiments, the spectra for g values near g_1 were calculated for a proton, while those to lower g values were calculated for a deuteron, with the ^{1}H and ^{2}H signals being displayed on a common axis through a scaling of the proton ENDOR shifts by the ratio (g_D/g_H). The ^{2}H quadrupole interaction was idealized as being axial, with the unique axis along the H−O bond (Table 1).

Figure 5b presents an optimized set of ^{1,2}H ENDOR spectra calculated using eq A3 under the alternate assumption that two inequivalent protons of a water are terminally bound to Fe^{III} (**T** model). As noted above, the hyperfine tensor for a terminal proton is predicted to be approximately axial and becomes effectively so for $\beta_1 \gtrsim 110°$ (Figure 3). We have simplified the problem by working in this limit, as the mildly anisotropic **g** tensor of **X** (*vide supra*) gives relatively poor orientation selection even at Q band, which does not permit an accurate determination of the small experimental deviations from axiality. In this case, the hyperfine tensor components for a proton depend almost exclusively on the Fe^{III}−H distance. The distances of the two protons to Fe^{III} were chosen by assuming that the maximimum calculated dipolar interaction for each one gives rise to one of the two largest doublet splittings in the

(39) Fann, Y.-C.; Ong, J.; Nocek, J. M.; Hoffman, B. M. *J. Am. Chem. Soc.* **1995**, *117*, 6109−6116.
(40) Fann, Y. C.; Gerber, N. C.; Osmulski, P. A.; Hager, L. P.; Sligar, S. G.; Hoffman, B. M. *J. Am. Chem. Soc.* **1994**, *116*, 5989−5990.

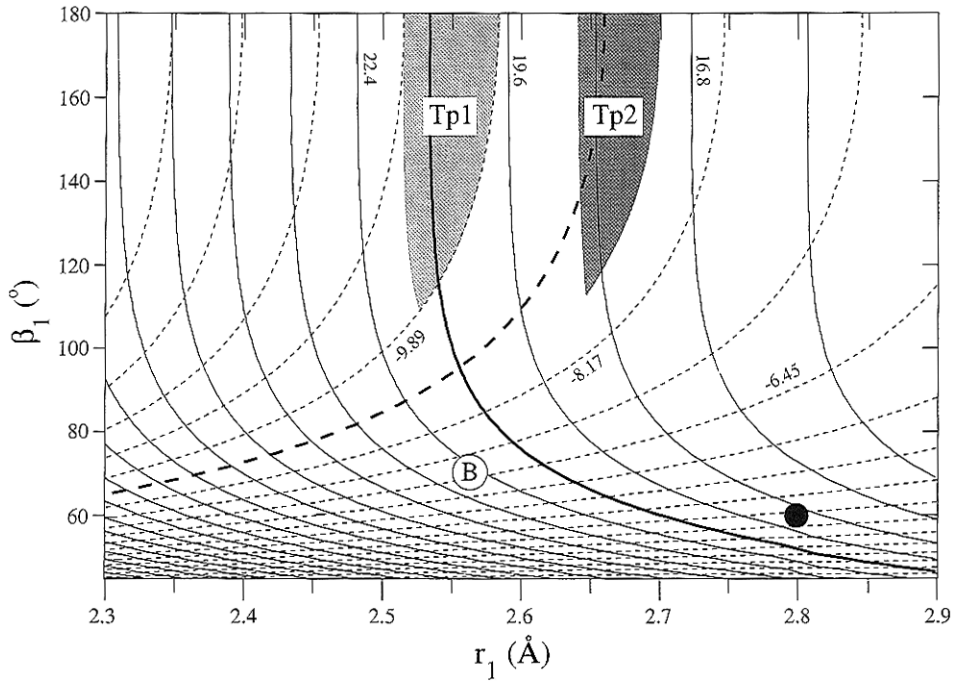

Figure 4. Contour plot of cluster hyperfine tensor **A** (eq A1) principal components A_3 (largest; solid line) and A_2 (smallest but second in magnitude; dashed line) as calculated with eq A3 for the metrical parameters r_1 and β_1 as defined in Figure 3, for a fixed $Fe^{III}-Fe^{IV}$ distance of 2.5 Å. Tp1 (Light-gray area): **T** (terminal) model, proton 1. Tp2 (dark-gray area): **T** model, proton 2 (see Table 1). B: **B** (bridge) model, symmetrical oxygen (○), see Table 1. **B** model, unsymmetrical oxygen (●), see text.

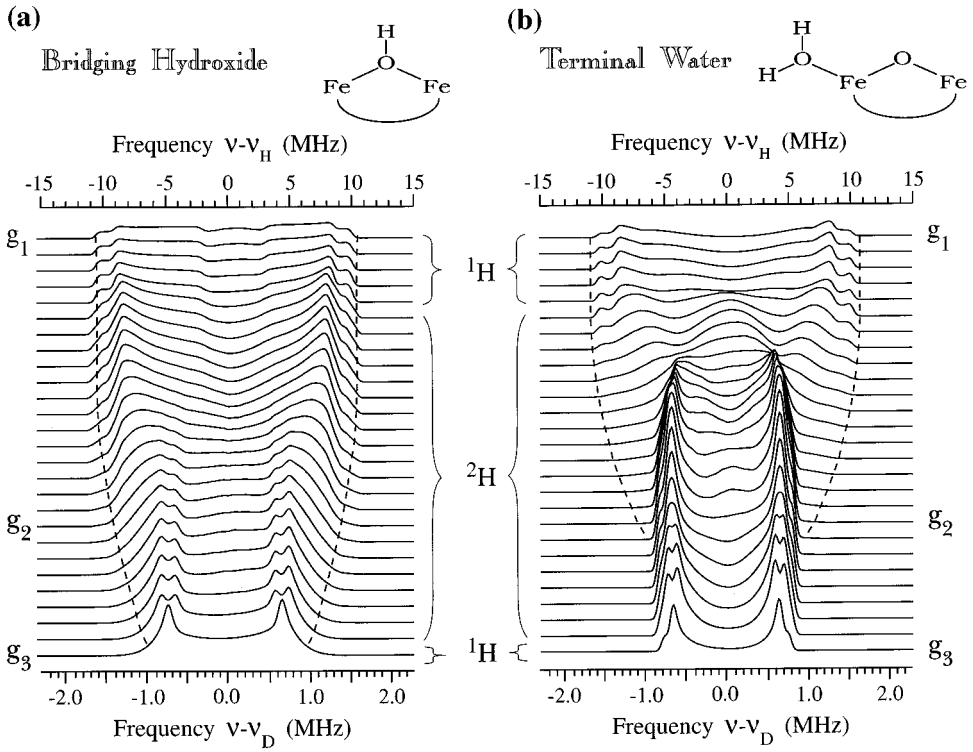

Figure 5. Optimized simulations of the field dependence of ^{1,2}H (as indicated) ENDOR responses for intermediate **X** within (a) the **B** model (bridging hydroxide, left), and (b) the **T** model (terminal water plus oxo bridge, right). The ^{1}H and ^{2}H signals are displayed in a common axis as ENDOR shifts from the Larmor frequency ($\Delta\nu$) through a scaling of the proton ENDOR shifts by the ratio g_D/g_H; all spectra have been centered around the nuclear Larmor frequency. The maximum breadth of the ENDOR pattern has been indicated by the dashed lines.

experiments (see below). The ranges of acceptable values for the locations of these protons are indicated by the two gray areas of Figure 4 and are quite reasonable for a bound water with Fe−O and O−H distances used in the bridging model. The two Fe−H distances chosen to best match the experimental splittings differ by only ∼4% (Table 1), corresponding to a minimally distorted water coordination. For example, if we begin by assuming an idealized tetrahedral disposition of protons and lone pairs about the O, with one lone pair coordinated to Fe^{III}, then such an inequality in Fe−H distances could come from as little as an ∼7° twist of the water about the bisector of the H−O−H angle. It is *not* possible to reproduce the breadth of the spectrum by assuming a terminal water bound to Fe^{IV} while using reasonable metrical parameters. According to eqs A1−A3 (Figure 4), the maximum hyperfine tensor component for a water attached to the Fe^{IV} ($S = 2$) ion would only be 8−10

Table 1. Metrical and [1,2]H Spin Hamiltonian Parameters Used To Calculate the 2-D ENDOR Patterns Displayed in Figure 3[a]

	B model[b]	**T** model	
		proton 1	proton 2
r_1 (Å)	2.56 ± 0.05	2.55 ± 0.03	2.67 ± 0.03
β_1 (deg)	72.3 ± 0.3	140−220	135−225

	B model[b]		**T** model[c]			
			proton 1		proton 2	
	^{1}H	^{2}H	^{1}H	^{2}H	^{1}H	^{2}H
A_1 (MHz)[d,e]	−17.5	−2.686	−10.25	−1.5745	−8.8	−1.3518
A_2 (MHz)	−9	−1.382	−10.25	−1.5745	−8.8	−1.3518
A_3 (MHz)	20.5	3.147	20.5	3.149	17.6	2.7035
ENDOR line width (MHz)[f]	0.5	0.07	0.5	0.07	0.5	0.07
EPR line width (MHz)[f]	90		35		35	

[a] Components of the hyperfine tensor **A** are calculated according to eqs A1 and A3; variations of these hyperfine components with the metrical parameters are plotted in Figure 4. Parameters are defined in Figure 3. Components of the ^{2}H quadrupole tensor, **P**, are idealized from those given for water in ref 43: $[P_1, P_2, P_3] = [-0.045, -0.045, 0.09]$ MHz. In other terminology, $e^2qQ = 2P_3 = 4$K and $\eta = 0$. Simulations employed $\mathbf{g} = [g_1, g_2, g_3] = [2.0081, 1.9977, 1.9926]$. [b] For model **B**, a small isotropic hyperfine component of $A_{iso}(^1H) = 2$ MHz improved the agreement with the experimental data and is included. [c] This model, as implemented ($\beta_1 > 90°$), is insensitive to Fe−Fe distances. As stated before, a value of 2.5 Å was used, which is in accordance to the EXAFS data. [d] The Euler angles for **A** in the **B** model are $\alpha = 50°$ and $\beta = 90°$. The Euler angles for **A** in the **T** model are as follows: proton 1, $\alpha = 10.3°$ and $\beta = 72.8°$; proton 2, $\alpha = 20°$ and $\beta = 90°$. For definition of angles, see ref 44. [e] The Euler angles for **P** of deuterons in the **B** model are $\alpha = 20°$ and $\beta = 90°$. The Euler angles for **P** of deuterons in the **T** model are as follows: proton 1, $\alpha = 45°$, $\beta = 61.1°$; proton 2, $\alpha = 70°$, $\beta = 90°$. [f] FWHM Gaussian.

MHz, not the 17−20 MHz for water bound to Fe^{III} ($S = {}^5/_2$), the difference coming from the coefficients in eq A1 ($^7/_3$ for Fe^{III}, but $-{}^4/_3$ for Fe^{IV}). We note explicitly that the model of a bound water is indistinguishable from one with a 2-fold disordered bound hydroxyl.

The hyperfine tensors for the two protons, and hence the water molecule itself, were oriented relative to **g** so as to achieve the best agreement under the constraint that they are related as part of a tetrahedral water molecule. The A_3 axis, and thus the bound water, lie roughly along the g_1 axis. The precise distances chosen, the resulting hyperfine tensor components, and the orientational parameters are listed in Table 1. The calculated 2-D pattern provided by the spectra calculated at fields across the EPR envelope of **X** (Figure 5b) again is a composite of ^{1}H and ^{2}H simulations, with ^{2}H quadrupole parameters chosen as in the **B** model.[41]

The parameters defining the **B** and **T** model calculations were chosen to generate sets of 2-D spectra that optimize the agreement with experiments presented below, and, as a result, the two sets are *constrained* to have important similarities. At g_1, each simulation shows a pair of proton doublets, with splittings of 16.8 and 19.6 MHz. In the **B** model, Figure 5a, these both arise from the single bridge proton, while in the **T** model, Figure 5b, each doublet is from a distinct proton terminal to Fe^{III}, with the two protons having slightly different Fe^{III}−H distances, as noted. The deuterium spectra also agree near g_3, in revealing a pair of sharp features, a doublet of doublets whose main splitting is approximately 1.38 MHz, with a minor splitting of about 0.12 MHz. However, there are a number of key differences between the models, as well. In the **B** model, the strongly coupled signals near g_1 exhibit smooth "*shoulders*", whereas the **T** model has "*peaklike*" features. Perhaps the most transparent difference between the two models is in the field dependence of the overall breadth of the ENDOR pattern at intermediate values of *g*. As indicated by the dashed lines in Figure 5, within the **T** model, the overall breadth decreases rapidly from its maximum value of ∼20 MHz (for ^{1}H; 3 MHz for ^{2}H) to approximately 9 MHz (1.38 MHz for ^{2}H) as the magnetic field is increased from g_1 to g_2. The pattern breadth then remains unchanged between g_2 and g_3. In contrast, model **B** predicts that the breadth of the pattern changes little between g_1 and g_2; then, as the magnetic field increases further, the width of the ENDOR pattern decreases slowly until at the g_3 edge of the spectrum it becomes ∼9 MHz. Although both models predict a sharp ∼9 MHz doublet of doublets near g_3, in the **T** model the secondary splitting reflects the fact that the two inequivalent protons have different hyperfine couplings for the g_3 orientation, and it occurs in both ^{1}H and ^{2}H calculations. In contrast, in the **B** model, the ^{1}H spectrum arises from a single hyperfine coupling to the unique bridge proton; the secondary splitting in the ^{2}H spectrum arises solely from the quadrupole interaction. Finally, in the **B** model, this 9 MHz doublet appears as a sharp feature only for fields between g_3 and g_2; the peaks broaden quickly as *g* increases toward g_1. In contrast, in the **T** model, the sharp pair of doublets persists from g_3 to *g* values well above g_2.

Use of Multiple ENDOR Techniques To Obtain Optimized [1,2]H Spectra. To distinguish between these two models requires the acquisition of a complete 2-D set of spectra from the exchangeable protons taken at fields across the EPR envelope of **X**.[31,37,38] These spectra must be collected in such a manner as to give reliable peak intensities and shapes as well as frequencies, so that the different predictions by the two models discussed above can be tested. This section indicates how the *combination* of CW *and* pulsed ENDOR measurements can answer these questions, although they are beyond the reach of any one protocol.

The ^{1,2}H ENDOR signals from exchangeable hydrogenic species associated with intermediate **X** exhibit hyperfine couplings that range from ∼20 MHz (for protons) to a fraction of a megahertz (for deuterons). For investigations of the exchangeable ^{1}H ENDOR signals that have $A \gtrsim 12$ MHz and do not overlap with the signals from nonexchangeable protons, namely the "wings" of the ENDOR pattern at fields in the vicinity of g_1, CW ENDOR is the technique of choice because it gives the best S/N, *provided* the shapes are not distorted by relaxation effects. As discussed in the Materials and Methods section, Davies pulsed ENDOR measurements, which are useful for such "larger" coupling constants and do give reliable peak shapes, were used to select the CW spectrometer settings that give proper shapes for the strongly-coupled exchangeable proton

(41) The relative orientations of the hyperfine and quadrupole tensors for each protonic species depend on the exact orientation of the water, with indistinguishable results for an appreciable range of choices; such details are irrelevant to this report.

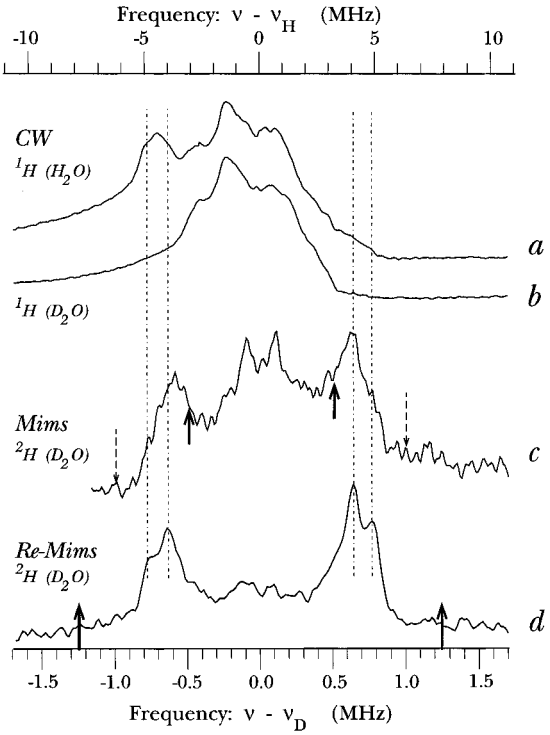

Figure 6. ^{1,2}H Q-band ENDOR spectra taken at $\approx g_3$ of **X** using each of the techniques employed in this study. The ^{1}H and ^{2}H signals are displayed in a common axis through a scaling of the proton ENDOR shifts by the ratio g_D/g_H; all spectra have been centered around the nuclear Larmor frequency (temperature, 2 K). (a) CW ^{1}H spectrum of intermediate **X** in H_2O buffer. Conditions: microwave frequency, 35.3 GHz; modulation amplitude, 8 G; modulation frequency, 100 kHz; rf scan speed, 1 MHz/s; rf frequency sweep, from high frequency to low. (b) CW proton spectrum of intermediate **X** in D_2O buffer. Experimental conditions are as in (a). (c) Mims ^{2}H pulsed ENDOR spectrum of intermediate **X** in D_2O buffer. Conditions: microwave frequency, 34.975 GHz; $\tau = 500$ ns; microwave pulse width, 28 ns; rf pulse width, 60 μs. The $n = 1$ Mims hole (eq 1) has been indicated by the dashed arrows; the points of maximum sensitivity have been indicated by the solid arrows. (d) ReMims ^{2}H pulsed ENDOR spectrum of intermediate **X** in D_2O buffer. Conditions: microwave frequency, 34.978 GHz; $\tau = 204$ ns; microwave pulse width, 28 ns; rf pulse width, 60 μs; $\tau_2 = 216$ ns. The rf frequency window has been indicated by the solid arrows. The $n = 1$ Mims "hole" (eq 1) is out of the frame; the points of maximum sensitivity have been indicated by the solid arrows.

signals near g_1. Although the Davies technique could not simply be used rather than CW ENDOR because it has poorer S/N, the pair of ^{1}H doublets with $A_H \approx 18-20$ MHz seen near g_1 were shown to have the same shapes when detected with the CW and Davies protocols.

We have reported that, when the ^{1}H signals from exchangeable protons overlap those from nonexchangeable protons, then the signal shapes obtained for the exchangeable ones by subtracting the spectra from samples in H_2O and D_2O buffers often are not reliable.[22] In this case, as explained in the Materials and Methods section, it is best to use the stimulated-echo Mims pulsed ENDOR technique to directly examine the ^{2}H signals from deuterons that have been exchanged into the sites of interest in D_2O buffer. However, the hyperfine selectivity of this technique, as manifest in eq 1, can cause difficulties in obtaining undistorted ^{2}H signals. These issues are illustrated in Figure 6 by the proton/deuteron ENDOR spectra taken near g_3, where the ^{1}H and ^{2}H signals are displayed on a common deuteron frequency axis through a scaling of the proton ENDOR shifts by the ratio g_D/g_H. Figure 6a shows the CW Q-band proton ENDOR spectrum near g_3 of intermediate **X** dissolved in H_2O; Figure 6b displays the proton ENDOR spectrum of the same compound in D_2O solvent. The CW spectra have good S/N but are unsymmetric around $\Delta\nu = 0$ MHz, as is often the case in Q-band CW ENDOR; in this instance, the ν_- branch ($\Delta\nu < 0$) is more clearly seen. Comparison of the two spectra shows that a proton signal in the range $-6 \le \Delta\nu \le -3.5$ MHz, corresponding to $A_H \approx 7-12$ MHz, has disappeared in the D_2O buffer (Figure 6b), proving that the proton(s) responsible for this signal are solvent exchangeable. Unfortunately, it is not possible to obtain a reliable shape for this feature by subtraction. Indeed, it is impossible to determine whether there is *any* exchangeable intensity in the long trailing edge to low frequency; in addition, the peak that is obviously lost upon exchange gives evidence of structure, but the structure is not well-resolved. The ν_+ signal ($\Delta\nu > 0$) at $3.5 \le \Delta\nu \le 6$ MHz is barely detectable and, thus, offers no assistance. Likewise, our experience shows that it is not possible to determine whether any intensity associated with couplings of, e.g., $A_H \lesssim 3$ MHz is lost upon solvent exchange.

A Mims pulse ENDOR deuteron spectrum near g_3 for intermediate **X** in D_2O buffer (Figure 6c), taken with $\tau = 500$ ns, shows the ^{2}H signals from exchangeable protons without an interfering background. The bold arrows indicate the frequencies of sensitivity maximum ($n = A\tau = 0.5$) for this value of τ, according to eq 1. In practice, this experiment is excellent for all hyperfine couplings, $A \lesssim 1$ MHz ($n \lesssim 0.5$). Thus, one sees the presence of a broad central feature, $A_D \lesssim 0.8$ MHz, with sharp inner lines at $\Delta\nu_D = \pm 0.1$ MHz ($A_D = 0.2$ MHz; $n = 0.04$), These inner lines can be assigned to "matrix" deuterium atoms (e.g., from the histidine−imidazole amino N−H, etc). However, in this experiment, the signals from nuclei where the hyperfine value approaches 2 MHz ($\eta > 1$) are strongly influenced by the hyperfine selectivity that is described by eq 1. As a result, it would be impossible to determine whether there are "wings", corresponding to even higher A value, because the region of interest falls essentially under the Mims hole around $A_D \approx 2$ MHz ($n = 1$). In addition, although this Mims spectrum clearly shows both the ν_+ and ν_- partners that correspond to the exchangeable peak at $\Delta\nu_H = 9$ MHz in the CW ^{1}H spectrum (Figures 6a,b), presumably because the portions of the ^{2}H signal that correspond to larger $\Delta\nu$ are severely attenuated as predicted by eq 1, the ^{2}H peaks do not show any additional structure.

Complete information requires additional spectra with a shorter value of τ, where the intensity maximum and Mims hole are moved to higher A. Because of the long effective deadtime for this sample, τ cannot be sufficiently shortened in a Mims experiment, but any desired value is feasible using the ReMims stimulated-echo pulsed ENDOR protocol.[36] As can be seen by comparing parts c and d of Figure 6 the use of a shorter interval ($\tau = 204$ ns) in the ReMims pulse sequence moves the intensity maximum outside the entire ^{2}H spectrum. The ^{2}H $\nu_\pm$ doublet corresponding to the $A_H \approx 9$ MHz feature in Figure 6a is well-resolved now and, in fact, is disclosed to be a doublet of doublets. This sensitivity to τ *requires* that the ^{2}H doublet of doublet contains contributions from deuterons with different hyperfine couplings and proves that the subsidiary splitting is *not* wholly the consequence of the ^{2}H quadrupole interaction, which does not enter into the τ dependence of eq 1; the two peaks that result from a quadrupole splitting would be jointly suppressed, causing an attenuation but not an apparent frequency shift. For completeness, note that the ^{2}H distant ENDOR signals with small A are severely suppressed with the shorter τ value in Figure 6d. Thus, just as the larger hyperfine couplings, $A_H \gtrsim 12$ MHz, are addressable by a combination of CW and Davies pulsed ENDOR techniques, for **X** the smaller couplings, $A_D \lesssim$

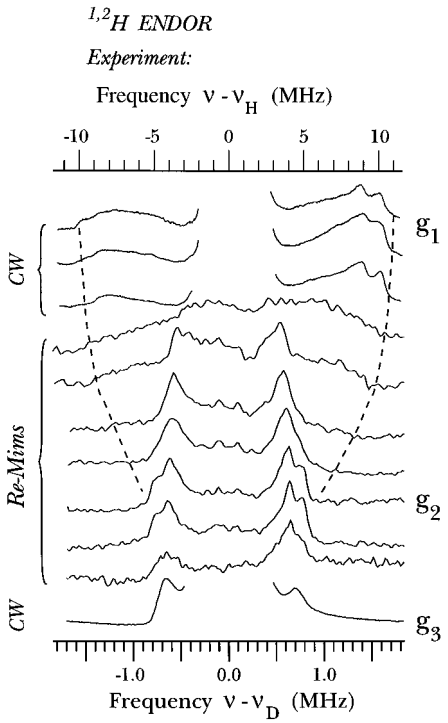

Figure 7. Experimental ^{1,2}H ENDOR spectra taken across the EPR envelope of **X**. The ^{1}H and ^{2}H signals are displayed in a common axis through a scaling of the proton ENDOR shifts by the ratio g_D/g_H; all spectra have been centered around the nuclear Larmor frequency (temperature, 2 K). The CW ^{1}H spectra come from a sample in H_2O buffer, and the pulsed ^{2}H spectra come from a sample in D_2O buffer. The maximum breadth of the ENDOR pattern has been indicated by the dashed lines, as in Figure 5. Conditions: CW, as in Figure 6a; ReMims pulse, as in Figure 6d.

1.85 MHz (corresponding to $A_H \lesssim 12$ MHz), are accessible through a combination of Mims and ReMims experiments.

Proton/Deuteron ENDOR of Intermediate X. An extensive 2-D set of experimental ^{1,2}H ENDOR spectra was taken across the EPR envelope of intermediate **X**. The spectrum at each field was taken by the appropriate technique, CW, Davies pulsed, or ReMims pulsed ENDOR, chosen so as to ensure that the intensities and shapes of the peaks associated with the strongly coupled exchangeable protons/deuterons are reliable: a portion of this data set is displayed in Figure 7. The input parameters (Table 1) for the model calculations presented in Figure 5, namely the metrical parameters of the protonated oxygenic species bound to the diiron center (Figure 2) and the orientation of the **g** tensor relative to the center, were optimized so as to make each model fit the experimental data as closely as possible, with particular focus on achieving the best possible match to spectra at the g_1 and g_3 edges of the EPR envelope. Comparison of the experimental results and the calculations permits a definitive conclusion that intermediate **X** contains a terminal water molecule (or 2-fold disordered hydroxyl; see above) bound to Fe^{III} and does not contain a hydroxyl bridge.

The above conclusions were reached by comparison of the two sets of calculations with the experiment and are based on the following observations. (i) Spectra taken near g_1 show a pair of strongly coupled doublets ($A_H \approx 19-20$ MHz) with peaklike features, not shoulders, in agreement with the **T** model and in opposition to the **B** model. (ii) As already stated, perhaps the most transparent difference between models seen in Figure 3 regards the field dependence of the maximum breadth of the ENDOR pattern. The breadth of the experimental pattern does not remain roughly constant at $A_H \approx 20$ MHz from g_1 to g_2 as in the **B** model but, as indicated, decreases from g_1 to g_2 and then remains constant at $A_H \approx 9$ MHz, as in **T**; *for fields between g_2 and g_3, there is no intensity from protons with $A_H \gtrsim 9$ MHz, in agreement with the **T** model and in opposition to the **B** model*. To be able to make this statement definitively required particular care. As shown by Figure 5, in the **B** model the signals with larger splittings in this field range have low intensity. However, the ReMims protocol permitted us to select a value of τ that optimizes the response to such signals; the baseline in this experiment is flawless, and extensive signal averaging produced spectra with good signal/noise ratios. Thus, even the low-intensity "wing" signals predicted by the **B** model would have been cleanly detected if they had been present. We conclude that they are not. (iii) The ^{2}H ReMims experiment with $\tau = 204$ ns reveals a sharp doublet of doublets with major splitting of $A_D \approx 1.38$ MHz near g_3, but the hyperfine selectivity shown by comparison to the spectrum with a larger value of $\tau = 500$ ns (Figure 6c) shows that this doublet is not simply a quadrupole splitting, as it would be in the **B** model, but reflects the unequal hyperfine couplings of the two inequivalent protons in the **T** model (see the discussion above). (iv) The doublet of doublets seen at g_3 persists from g_3 to g values substantially greater than g_2, rather than abruptly broadening and disappearing at fields near g_2; this, again, is in accord with the **T** but not the **B** model. (v) For clarity, we emphasize that the absence in the experimental ^{1,2}H spectra of *any* unexplained features with the large hyperfine couplings *required* for the proton of a bridging hydroxyl precludes there being both a bridging hydroxyl and a water molecule. (vi) Finally, we may comment on the possibility of an additional H_xO terminally bound to the Fe^{IV}, which would have small ^{1,2}H couplings. The current data give no evidence of such a species but neither disprove nor prove its presence; future ^{17}O ENDOR measurements will address this issue.

Conclusions

The striking agreement between the 2D set of experimentally optimized Q-band ^{1,2}H ENDOR spectra in Figure 7 and the simulations based on the **T** model displayed in the right diagram in Figure 5 show that the exchangeable proton signals displayed by intermediate **X**, belong to two protons associated with a terminal water bound to Fe^{III}. Table 1 presents the principal values and orientations of the hyperfine tensors for both protons, along with the metrical parameters describing the terminal water model. Within the precision of the modeling, this picture is indistinguishable from that of a 2-fold disordered terminal hydroxyl; ESEEM experiments will address this issue.

The strong spin-coupling between the iron ions and the short Fe−Fe separation observed by EXAFS spectroscopy requires that intermediate **X** contain one or more oxo/hydroxo bridges. The determination that **X** does not have a hydroxyl bridge, in conjunction with the finding of a terminal water, then establishes that intermediate **X** contains the $[(H_2O)Fe^{III}OFe^{IV}]$ fragment that defines the **T** model (Figure 1). The presence or absence of the second oxo bridge of a diamond core, a determination of the fate of the two atoms of dioxygen, and a confirmation that there is not a second H_2O bound to Fe^{IV} will be the subject of a detailed report of ^{17}O ENDOR measurements using enriched solvent and gas.

Acknowledgment. The authors would like to express their gratitude toward C. E. Davoust for his extensive technical support and to the NIH (Grants HL 13531 (B.M.H) and GM 29595 (J.S.)).

Appendix: Hyperfine Tensor for a Proton Dipole-Coupled to an Antiferromagnetically Coupled ($S = {}^5/_2$; $S = 2$) Binuclear Center

Intermediate **X** is a diiron $S = {}^1/_2$ center comprised of an Fe^{III} ($S = {}^5/_2$) ion antiferromagnetically coupled to a Fe^{IV} ($S = 2$) ion.[27] As has been discussed extensively (Hendrich et al.,[42] DeRose and Hoffman[23]), a nucleus of a diiron center that has hyperfine couplings to the individual ferric and ferryl iron ions of $A_{Fe(III)}$ and $A_{Fe(IV)}$, respectively, will have an observed cluster hyperfine coupling matrix to the cluster spin, A_{obs}, that is a weighted sum of the individual ion interactions (eq A1),

$$\mathbf{A}_{obs} = \frac{7}{3}\mathbf{A}_{Fe(III)} - \frac{4}{3}\mathbf{A}_{Fe(IV)} \tag{A1}$$

Our previous work[23,39,40] has shown that the ENDOR patterns for a proton attached to an oxygenic species bound to iron (terminal water, bridging hydroxo) can be understood if $A_{Fe(III)}$ and $A_{Fe(IV)}$ are taken to be point−dipole interactions between the proton and the localized spins on the individual iron ions. We therefore considered a nucleus at an arbitrary location, as depicted in Figure 4, took the classical form of the point−dipole interaction with the individual uncoupled iron ions, ($A_{Fe(III)}$ and $A_{Fe(IV)}$ in eq A1), expressed them in the common axis frame of Figure 4, and added them according to eq A1 to obtain the effective hyperfine tensor **A** for the $S = {}^1/_2$ ground state Hamiltonian of the spin-coupled cluster system.[45] To carry this out, it is convenient to define a right-handed coordinate frame (**e**), the unit vectors of which are e_3, lying parallel to Fe−Fe; e_1, lying in the Fe(H)Fe plane perpendicular to e_3; and e_2, normal to the plane. As expressed in this frame, the cluster hyperfine interaction matrix takes the form given in eq A2:

$$\boldsymbol{A} = \begin{pmatrix} A_1\cos^2\gamma + A_3\sin^2\gamma & 0 & (A_1 - A_3)\sin\gamma\cos\gamma \\ 0 & A_2 & 0 \\ (A_1 - A_3)\sin\gamma\cos\gamma & 0 & A_1\sin^2\gamma + A_3\cos^2\gamma \end{pmatrix} \tag{A2}$$

This corresponds to the matrix for an interaction with principal values, $\mathbf{A} = [A_1, A_2, A_3]$, where the hyperfine frame is rotated relative to the molecular $[e_1, e_2, e_3]$ frame by a rotation around e_2 through the angle γ. This dipolar interaction matrix depends on the metrical parameters for the center, and we chose to parametrize **A** for a given geometry of Fe(H)Fe in terms of r_1, d_{Fe-Fe}, and the angle β_1 that is subtended by the Fe^{III}−H and Fe−Fe vectors (Figure 4). The principal values of the dipolar interaction tensor **A** then are given in eq A3, where r_1 is the distance between the Fe^{III} and the proton and r_2 is the distance between the Fe^{IV} and the proton:

$$t_1 = \frac{7}{3}\left(\frac{2g\beta g_n\beta_n}{r_1^3}\right) \qquad t_2 = -\frac{4}{3}\left(\frac{2g\beta g_n\beta_n}{r_2^3}\right)$$

$$\tan 2\gamma = \frac{[t_1 \sin 2\beta_1 + t_2 \sin 2\beta_2]}{[t_1 \cos 2\beta_1 + t_2 \cos 2\beta_2]} \tag{A3}$$

$$A_1 = \frac{1}{2}\left[\left(\frac{t_1 + t_2}{2}\right) + \frac{3}{2}\frac{1}{\cos 2\gamma}(t_1 \cos 2\beta_1 + t_2 \cos 2\beta_2)\right]$$

$$A_2 = -\frac{1}{2}(t_1 + t_2)$$

$$A_3 = -(A_1 + A_2)$$

With these equations, it is possible to calculate **A** for a proton at any position relative to the Fe−Fe framework; this, in turn, allows us to simulate a 2-D set of ENDOR spectra for the proton at multiple fields across the EPR envelope. Calculations with these formulas show that, when the proton lies outside of the region between the two iron ions ($\beta_1 \gtrsim 90$ or $\beta_2 \lesssim 90$), namely when it is part of a terminal ligand to one ion, then, to a good approximation, this result reduces to a point−dipole interaction with the adjacent iron. When the nucleus is located symmetrically relative to the two iron ions, namely when it is associated with an hydroxo (or aquo) bridge, then these results reduce to those reported previously.[23] For coupling of ions with different spins, only the coefficient in eqs A1 and A3 change.

JA9709942

(42) Hendrich, M. P.; Fox, B. G.; Andersson, K. K.; Debrunner, P. G.; Lipscomb, J. D. *J. Biol. Chem.* **1992**, *267*, 261−269.

(43) Edmonds, D. T. *Phys. Lett.* **1977**, *C29*, 233−290.

(44) True, A. E.; Nelson, M. J.; Venters, R. A.; Orme-Johnson, W. H.; Hoffman, B. M. *J. Am. Chem. Soc.* **1988**, *110*, 1935−1943.

(45) **Note Added in Proof:** The problem of a proton dipole-coupled to a dinuclear center has been treated recently by others. (a) Randall, D. W.; Gelasco, A.; Caudle, M. T.; Pecoraro, V. L.; Britt, R. D. *J. Am. Chem. Soc.* **1997**, *119*, 4481−4491. (b) Fiege, R.; Zweygart, W.; Bittl, R.; Adir, N.; Renger, G.; Lubitz, W. *Photosynthesis Res.* **1996**, *48*, 227−237.